A Neural Network-Based Power Mismatch Elimination Strategy for Integrated Solar and ESS ac/dc Systems (MARS)

Qianxue Xia, *Member, IEEE*, Suman Debnath, *Senior Member, IEEE*, and Maryam Saeedifard, *Fellow, IEEE*

***Abstract*— The multi-port autonomous reconfigurable solar power plant (MARS) is a promising concept for the integration of photovoltaic (PV) and energy storage system (ESS) to the transmission ac grid and a high-voltage direct current (HVdc) link. The presence of PV and ESS in each arm of the MARS results in uneven distribution of active power among different submodules (SMs), thereby leading to unbalanced SM capacitor voltages and potentially compromising the system stability. Moreover, in the case of partial shadings, shaded PV SMs will suffer from decreased power injections causing power mismatch in the MARS system. To address this issue, a neural-network-based power mismatch elimination (NNPME) strategy is proposed in this paper. The proposed NNPME strategy optimizes ESS usage and leverages both dc and ac circulating currents to facilitate power transfer among the SMs, arms, and phases of the MARS system. Simulation and control hardware-in-the-loop (cHIL) experiments demonstrate the effectiveness of the proposed NNPME strategy. Compared to the traditional approaches, the proposed NNPME strategy can significantly enhance system efficiency and ensure stable and continuous operation, even in the presence of uneven power distribution within the MARS system.**

***Index Terms*—Capacitor voltage balancing, Energy storage system, Photovoltaic, Power mismatch, Neural Network.**

I. INTRODUCTION

Today's electric power systems are undergoing a transition towards low carbon emission, marked by an increased presence of renewable energy resources. Among those resources, large-scale photovoltaic (PV) systems are experiencing a rapid growth. However, the intermittent nature of PV power generation poses challenges in the power system due to output power fluctuations. A well-established solution to address those challenges is to couple the PV power with an energy storage system (ESS) [1][2]. Among the power electronics architectures explored for this purpose, the modular multilevel converter (MMC) has been employed to integrate PV and ESS into a high-voltage direct current (HVdc) link [3][4]. Nevertheless, there is a limited body of research on the architectures required to seamlessly integrate PV and ESS into both HVdc links and the transmission ac grid. The multi-port autonomous reconfigurable solar power plant (MARS) offers power electronics and control architectures designed to effectively integrate PV and ESS into an HVdc link and a transmission ac grid [5].

One of the significant challenges associated with the MARS-type architecture, which includes both standard submodules (SMs) and SMs with external power sources, is maintaining the energy balance of the SM capacitors. This discrepancy in power consumption or production among SMs, referred to as inter-SM power mismatch in this paper, limits the operational range of the system. This mismatch leads to capacitor voltage imbalances that jeopardize the safe and reliable operation of MARS-type architectures. Although the widely used SM capacitor voltage sorting algorithm can handle this issue to some extent, it falls short when different types of SMs (with different power sources) are present in the same arm. In reference [6], a criteria vector is formulated to delineate the boundary of operating conditions for the MMC-based ESS to function properly. This analysis, however, is conservative and only suitable for systems with a single type of external power source. Reference [7] explores the power flow of the MMC with ESS integrated into the SMs and introduces a method to maintain the SM capacitor voltage balance by injecting dc and circulating currents. In the technical literature, circulating current injection has been widely adopted for internal control purposes of MMC-based PV or ESS systems, as it can address SM capacitor voltage imbalances [5][8], reduce SM capacitor voltage ripples [9][10], and eliminate inter-phase or inter-arm power mismatch [5][7][11] without affecting the grid current. Nevertheless, this approach also leads to increased current stress on the switching components, heightened fluctuations in SM capacitor voltages, and elevated conduction losses. Determining the optimal injected circulating currents can significantly enhance operational performance.

While the literature has analyzed the relationship between the MARS system arm power and circulating current references [7][11][12], it has not thoroughly discussed the precise correlation between SM capacitor voltage ripples and circulating current. Furthermore, the stability of the proportional-integral (PI)-based and/or proportional-integral

This work was supported by the U.S. Department of Energy, Office of Energy Efficiency and Renewable Energy under Solar Energy Technologies Office Agreement Number 34019. This manuscript has been authored by UT-Battelle, LLC under Contract No. DE-AC05-00OR22725 with the U.S. Department of Energy. The United States Government retains and the publisher, by accepting the article for publication, acknowledges that the United States Government retains a non-exclusive, paidup, irrevocable, world-wide license to publish or reproduce the published form of this manuscript, or allow others to do so, for United States Government purposes. The Department of Energy will provide public access to these results of federally sponsored research in accordance with the DOE Public Access Plan(http://energy.gov/downloads/doe-public-access-plan).

Qianxue Xia, was with Georgia Institute of Technology, GA 30332 USA. She is now with Oak Ridge National Laboratory, Knoxville, TN 37932 USA (email: xiaq@ornl.gov). Suman Debnath is with Oak Ridge National Laboratory, Knoxville, TN 37932, USA (email: debnaths@ornl.gov). Maryam Saeedifard is with the Electrical Engineering Department, Georgia Institute of Technology, GA, 30332 USA email: maryam@ece.gatech.edu).

differential (PID)-based control in [5][7][11][12] cannot be guaranteed, as the theoretical foundation is insufficient to explicitly derive circulating current references for controlling both ac and dc part of the SM capacitor voltage ripples. Additionally, for multi-objective optimization problems aiming to simultaneously minimize the circulating current and capacitor voltage ripples, PI-based control with static gains cannot adaptively control the magnitude of the injected circulating current under different operating conditions. Therefore, a novel control approach is imperative to ensure balanced energy distribution across different SM capacitors. Data-driven control has emerged as a promising technique in power converter-based systems, favored for its ability to function without complex mathematical modelling of nonlinear dynamics, and its rapid inference capability that is well-suited for real-time applications. Two major applications of data-driven control in power converters include machine learning (ML)-based linear control and ML-based nonlinear control. In the context of ML-based linear control, ML assists in dynamically adapting the control parameters of PI and/or proportional-resonant (PR) controllers according to different operating conditions, as exemplified by the artificial neural network (ANN)-aided PI controller proposed in [13] for adaptive control of a converter-based hybrid energy storage system. Additionally, neural networks have been trained to directly replace adaptive controllers [14]. In the realm of nonlinear control, such as model predictive control (MPC), several studies [14]-[18] have investigated the use of ANNs to emulate the behavior of MPC for the MMCs. This approach aims to substitute traditional MPC with a NN algorithm, thus reducing computational demands. Weight tuning is another application of data-driven methods in nonlinear control, enhancing the efficacy of control design [19]. Beyond their use in nonlinear control, data-driven methods are widely applied in voltage estimation [20] and fault diagnosis [21][22] for MMC applications. In reference [23], the authors utilize an NN to analyze the relationship between circulating currents, capacitor voltages, and grid dip severity. The research in [23] is directed towards improving the robustness of MMCs under unbalanced grid faults by using NN algorithms. Despite these advancements, studies applying NN to control more complex systems like MARS are still lacking.

The second challenge pertains to the unequal aggregated power generated by the external sources injected into the arms of the MARS-type system, referred to as inter-arm or inter-phase power mismatch in this paper. This discrepancy may potentially violate the limitation specified in the IEEE 1547 standard, which addresses current distortion resulting from the injection of unbalanced currents into the grid. The power mismatch between arms and phases has been explored in [24]-[33]. In [24], a circulating current-based approach is used to address arm and phase power mismatch in large-scale MMC-based charging stations. A load management algorithm is proposed to minimize the DC circulating current. In [25], power mismatches in the MMC-based PV system are mitigated by continually injecting circulating current. However, this continuous injection leads to additional power losses. The authors of [26] used a MARS-like architecture with both PV and battery SMs in each arm. The battery serves as a backup power source for PV according to grid dispatching. However, it is assumed that the battery rating is high enough to cover the PV output, which is not feasible in large PV plants. Additionally, no power mismatch control was considered. The authors in [27] analyze control methods to eliminate power mismatch in a hybrid MMC-based PV and ESS. They utilize an ESS system, along with dc and ac circulating currents, to mitigate power discrepancies between arms and legs. Reference [28] enhances the injected circulating current by adjusting the terminal voltage of the MMC-based PV system in response to power mismatch. However, this method has limited capability in eliminating the mismatched power and lacks a mathematical basis to justify the stability and effectiveness of the designed parameters. Furthermore, it does not address inter-SM power mismatches, and the optimal allocation of all sources is not ensured. The author of [29] proposed a circuit configuration for an MMC-based PV system which parallels the upper and lower SMs of each phase to the same set of PV arrays to eliminate the arm power unbalance. Similarly, [30] adopted this circuit topology and used dc circulating current control to balance PV power unbalance and utilized arm voltage compensation for unbalanced vorlage sags. However, no theoretical proof is provided to demonstrate the efficiency of this topology. Additionally, factors such as faulty cells or dust layer accumulation, which can cause inter-arm or inter-submodule power mismatches, still need to be addressed. In the circulating current-based approach described above, the MMC-based system also faces challenges with additional power loss and overcurrent issues. Reference [31] enhances the performance of MMC-PV system under PV power imbalance conditions by adjusting the upper boundary of the modulation index, which may not be suitable for nearest level control. Reference [32] proposed a novel two fundamental frequency zero-sequence voltage injection for phase power mismatch and an independent arm power control technique is proposed for arm power mismatch. However, since there is only one type of SM, and the assumption that the MMC arm can be considered as two independent voltage sources, no inter-SM power mismatch is considered. Therefore, this approach may not be suitable for systems like MARS. None of the existing studies [25]-[32] take into account the presence of normal SMs, nor do they ensure the optimal allocation of all sources. Thus, in [33], a redundant module is introduced to compensate for the fluctuating voltage of PV SMs caused by partial shading. This module improves the quality of output power to the grid under partial shading by individually controlling the PV SMs, which may not be suitable for systems with a large number of SMs. Notably, there is substantial gap in the existing literature concerning MARS-type architectures that integrate two or more external power sources alongside the SMs and has three types of SMs in one arm.

The aforementioned discussion highlights the need for a simple, efficient, and easily generalizable control method for MARS-type systems that incorporate multiple power sources.

To address this research gap, this paper proposes a neural network-based power mismatch elimination (NNPME) strategy, which integrates as the power management module with the NN-based EBC, enhancing operational efficiency, increasing operational versatility, and reducing the need for excess additional injected currents for MARS-type systems. The contribution of this work are as follows: (i) providing a detailed analysis of inter-SM, inter-phase, and inter-arm power mismatches and proposes an efficient power management system; (ii) proposing a novel NN-based energy balancing control (EBC) that augments the operational efficiency of MARS and minimizes additional injected currents; (iii) carefully contrasting the random forest (RF), ANN and the nonlinear autoregressive exogenous (NARX) neural network models with benchmark PI control, highlighting their capability to minimize the required additional injected currents.

II. MARS Circuit and the Hierarchical Control

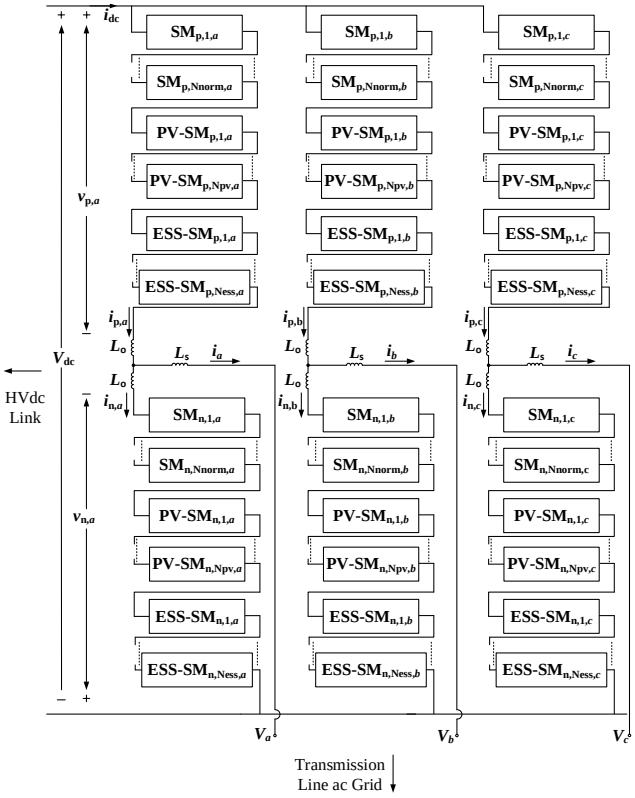

Fig. 1. MARS circuit architecture.

The MARS circuit architecture is illustrated in Fig. 1. Each arm of the MARS system incorporates three categories of SMs, normal SMs, PV SMs, and ESS SMs. Each of the three types of SMs is equipped with a front-end half-bridge circuit. The PV SMs and ESS SMs feature dc-dc converters that connect to the dc-link of the half-bridge. The multi-faceted control objectives of the MARS involve tracking power dispatch commands, ensuring continuity of operation under low short circuit ratio conditions, and providing fast frequency support in case of generation loss. To achieve these objectives, a hierarchical control system is employed, comprising L1, L2, and L3 controllers. The detailed implementation of L1 controller is depicted in [5] and shown in Fig. 2, it includes dq current control, virtual synchronous generator (VSG) which is detailed in [5], the proposed power management module and the NN-based EBC. The power management module determines the reference power commands of PV and ESS based on the power dispatch command, additional power requirements (ΔP and ΔQ) from the VSG control of MARS, the maximum available PV power ($P_{\mathrm{pv,MPPT}}$), and the power rating of the ESS SMs ($P_{\mathrm{ess,rating}}$). It also generates the dc-reference command sent to the dc-current controller, which plays a crucial role in power mismatch elimination. The proposed NN-based EBC along with the power management module constitutes the proposed NNPME. The arm modulation indices (m_{arm}), generated based on the L1 controller, are forwarded to the L2 controller. The L2 controller includes a capacitor voltage balancing control [34] and the nearest level control. The L3 controller, exclusively employed in the PV and ESS SMs, is responsible for regulating the power transferred from the PV and ESS.

III. Inter-SM Power Mismatch Elimination

The presence of multiple PV arrays and ESS in the MARS SMs introduces the potential for power imbalances due to unequal power injection from different types of SMs within one arm. Under specific operating conditions characterized by low or negative dc currents, the primary consequence of inter-SM power mismatches is the emergence of disparities in capacitor voltages. Conventional MMC capacitor voltage balancing algorithms, which rely on sorting techniques, may prove insufficient in addressing these imbalances in MARS-type systems with multiple energy inputs to individual SMs [13]. In existing literature, analytical equations have been put forth to model the dynamics of SM capacitor voltage ripples. However, these models lose validity when analyzing SM capacitor voltage differences defined as $\sum(V_{c\sigma})^2$ in (1), primarily because the assumption of balanced capacitor voltages does not apply in such cases. This introduces complexity when attempting to establish a clear relationship between $\sum(V_{c\sigma})^2$ and the circulating current. Consequently, designing a PI-based EBC not only becomes challenging but may also fall short of ensuring stable operation of the converter under all scenarios. To address these limitations, this paper proposes an NN-based EBC control. The proposed NN-EBC targets the mitigation of these voltage discrepancies inherent to the complex MARS configuration.

In the MARS system, upper and lower limits for capacitor voltages are established based on designed stability constraints. The lower limit ensures stable operation of the connected boost-type dc-dc converter in the L3 controller, while the upper limit prevents over-voltage stress on the switches. Operating conditions where SM capacitor voltages fall within these limits are considered stable. Furthermore, it is essential to limit the dc current ripple to less than a certain percentage of the nominal current to guarantee stable operation. In this paper, this percentage tolerance is assumed to be 20% as a design requirement. A 20% tolerance for dc current ripple is establish-

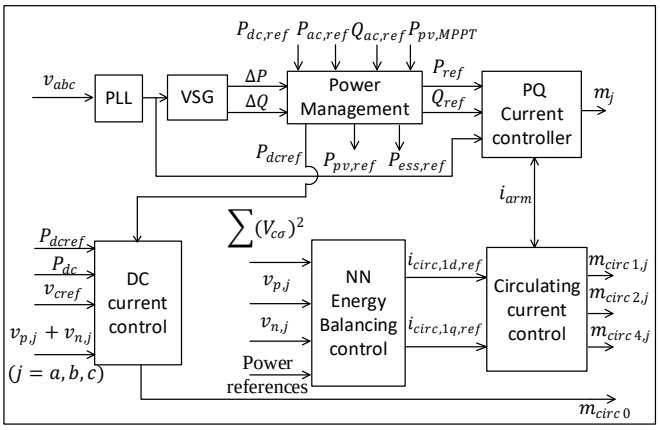

Fig. 2. L1 controller diagram with NN-based EBC.

-ed as a key design requirement for the system. Current HVDC standards [35][36] specify requirements for dc-side voltage harmonics but do not address dc current ripple. Therefore, this 20% tolerance is derived based on several critical considerations, including simulation results focusing on the stability of the internal MARS system and the operational specifications of the selected power devices. The chosen power devices are designed to operate reliably within this ripple range without degrading performance. The tolerance level has been validated through extensive simulations and cHIL experiments, ensuring stable operation of the internal MARS system. Additionally, adhering to this tolerance helps mitigate the risks of excessive heating and potential device failures. For an operating condition to be considered stable, both the capacitor voltage limits and dc current ripple restrictions must be satisfied simultaneously.

$$\sum(V_{c\sigma})^2 = \sum_{i=1}^{N}(v_{c,p,i,a} - \frac{v_{p,a}}{N})^2 + \sum_{i=1}^{N}(v_{c,n,i,a} - \frac{v_{n,a}}{N})^2 + \sum_{i=1}^{N}(v_{c,p,i,b} - \frac{v_{p,b}}{N})^2 + \sum_{i=1}^{N}(v_{c,n,i,b} - \frac{v_{n,b}}{N})^2 + \sum_{i=1}^{N}(v_{c,p,i,c} - \frac{v_{p,c}}{N})^2 + \sum_{i=1}^{N}(v_{c,n,i,c} - \frac{v_{n,c}}{N})^2 \quad (1)$$

where $v_{c,p\,(n),i,a}$ is the i-th SM capacitor voltage of the upper (lower) arm "p" ("n") for a given phase a. $\sum(V_{c\sigma})^2$ captures deviation of all SM capacitor voltages from the average voltage.

IV. ML-Based EBC

A. Data Driven Methods

Due to inherent complexity of the system, the dynamics of the MARS system employed for EBC tuning exhibit non-linear behavior. Furthermore, the conventional PI-based EBC design relies on inferences drawn from simulation results, posing challenges in effectively tuning the gains to ensure stability and optimal performance across a range of operating conditions. The traditional PI-based EBC approach, while limited in its ability to mitigate mismatched power, lacks a solid mathematical foundation for justifying the stability and effectiveness of the selected parameters. To address these limitations and ensure adaptability of the EBC for the MARS system under various operating conditions, while concurrently reducing circulating current, it is imperative to tackle a complex multi-objective optimization problem. The control parameters, comprising the gains in the PI controller, offer limited degrees of freedom to achieve all desired objectives. In [13], where the PI-based EBC is implemented, each set of gains undergoes rigorous testing under a minimum of 2000 operating conditions to ensure proper design. However, an optimal set of gains for one specific condition might not necessarily be optimal for another, particularly with regards to minimizing the circulating current. This can lead to scenarios where circulating currents are unnecessarily high to maintain system stability. To address this issue, data driven EBC methods are proposed. These methods can be trained across a diverse set of operating conditions to comprehend the intricate system dynamics, enabling it to predict optimal circulating current references. Based on the PI-based EBC, the ML-based data-driven methods capture the relationship between the circulating reference and active power, reactive power, dc power, capacitor voltage mismatch, etc. as expressed by:

$$\begin{aligned}(i_{circ,1d,ref}, i_{circ,1q,ref}) = y = F(x) \quad (2)\\ = F(P_{ac}, P_{dc}, Q_{ac}, \sum|v_{c\delta}|^2, v_{p,j} - v_{n,j})\end{aligned}$$

where P_{ac}, P_{dc} and Q_{ac} represent the power dispatch commands, $v_{p,j} - v_{n,j}$ signifies the arm capacitor voltage mismatch. The control variables $i_{circ,1d,ref}$ and $i_{circ,1q,ref}$ denote the fundamental circulating current references based on the *dq* reference frame. The block diagram of the PI-based EBC is depicted in Fig. 3, with (3) in Fig. 3 given by:

$$i_{circ,1d,ref} = \frac{2v_{y,j}}{3}(P_{da,ref} + P_{db,ref} + P_{dc,ref}) \quad (3a)$$

$$i_{circ,1q,ref} = \frac{2v_{y,j}}{3}(Q_{da,ref} + Q_{db,ref} + Q_{dc,ref}) \quad (3b)$$

where $P_{da,ref}, P_{db,ref}, and\ P_{dc,ref}$ represent the references of real power transferred from the upper phase arm to the lower phase arm of the three phase legs. $Q_{da,ref}, Q_{db,ref}, and\ Q_{dc,ref}$ are the reactive powers transferred from the upper phase arm to the lower phase arm of the three phase legs.

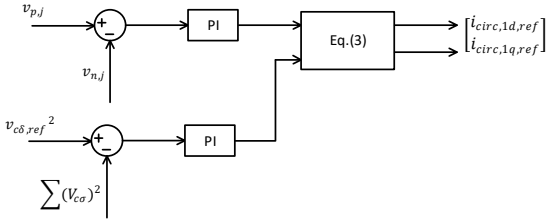

Fig. 3. Block diagram of PI-based EBC.

To clarify the data acquisition and training procedures of the ML models, all the steps are illustrated in Fig. 4 and further elaborated in the following subsections.

B. Data Acquisition and Model Training

The dataset is generated through the simulation of a high-fidelity MARS model [5]. The inputs for the MARS model include P_{ac}, P_{dc} and Q_{ac} as well as $i_{circ,1d,ref}$ and $i_{circ,1q,ref}$. These inputs are systematically swept to obtain the corresponding model outputs, which include $\sum|v_{c\delta}|^2$ and $v_{p,j} - v_{n,j}$. The data acquisition process is depicted in Fig. 5. P_{ac} is sampled across a range of [-400, 400] MW in 20 MW increments. The dc power reference, P_{dc}, is sampled from [-300, 300] MW with the same 20 MW step size. Reactive power, Q_{ac}, is sampled within [-300, 300] MVar in 75 MVar increme-

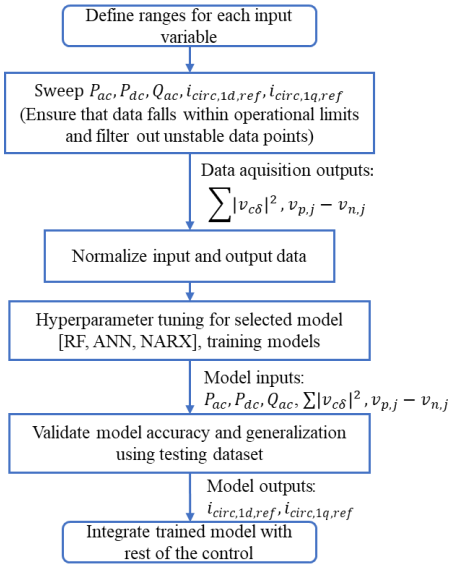

Fig. 4. The flowchart of data acquisition and training of ML models.

-nts. These ranges are selected to account for various active and reactive power demands and their impact on system stability. Before analysis, these operating conditions are filtered based on ESS and PV ratings to ensure they remain within the system's limits.

Due to limitations in computational resources, the d-axis and q-axis circulating currents are swept based on the circulating current references generated by the PI-EBC controller. The lower magnitude of the circulating current generated by the PI controller is swept. Circulating current settings that cause unstable simulation results are filtered out within the first 0.2 seconds. The stable, lower magnitude circulating currents that satisfy the stability criteria are retained in the dataset. In total, 6,300 such carefully selected samples are utilized in the training phase. This selective sampling approach ensures that the trained neural network model can effectively minimize the magnitude of injected circulating currents under diverse operating conditions, ultimately enhancing the efficiency of MARS-type systems.

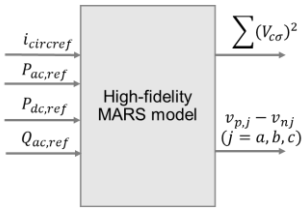

Fig. 5. Data acquisition process.

An additional dataset of 2500 samples are used for the testing process of the neural networks. The testing dataset includes the following operating conditions: The active reference power P_{ac} is sampled within a range of [-400, 365] MW with a step of 45 MW. The dc power reference P_{dc} is sampled from [-300, 285] MW with a step of 45 MW. The reactive power reference Q_{ac}, ranges from [-300, 285] MVar with a step of 45 MVar. These operating conditions are first filtered based on the ESS and PV ratings to ensure they fall within the system's operational limits, retaining only 2500 stable operating conditions for the testing dataset.

Prior to training the models, several preprocessing steps are applied to the data to ensure accurate and stable model predictions. All input and output data are normalized to a standard range, typically between 0 and 1, to ensure uniformity and improve the convergence rate during training. Unstable operating conditions and outliers are filtered out to ensure that only stable and relevant data are used for training. This helps in avoiding the inclusion of noise and anomalies in the dataset.

C. RF-based EBC

RF is a widely recognized ML method in the industry, known for its efficacy in dealing with nonlinear systems and minimal tuning requirements. It is the first model employed for the controller. The random forest regressor model is employed, and the two hyperparameters, number of estimators and maximum depth, are tuned using the grid search method.

D. NN-based EBC

ANNs are particularly effective for regression fitting problems as they can model complex, non-linear relationships between input and output variables. This makes them ideal for tasks where the goal is to predict a continuous output based on a set of input features. By selecting appropriate architectures (such as the number of layers and neurons), ANNs can be designed to avoid overfitting. Additionally, ANNs have relatively few hyperparameters to tune compared to more complex models, making them easier to optimize and deploy in control systems.

To optimize the performance of the ANN model, the grid search algorithm is employed for hyperparameter tuning. Various network configurations including different numbers of layers are explored to identify the optimal depth. Various numbers of neurons per layer are tested to find the configuration that provides the best balance between accuracy and computational efficiency. Different activation functions, such as ReLU, sigmoid, and tanh are evaluated to determine which one best facilitates effective learning and performance. Additionally, a range of learning rates is tested to identify the optimal rate that ensures efficient converge without overshooting. The optimal model comprises a three-layer fully connected network with 12 neurons in the hidden layer. The proposed ANN model architecture is illustrated in Fig. 6.

Both the hidden layer and the output layer utilize activation functions. The output of neuron *j* in layer *d+1* could be declared as:

$$y_j^{d+1} = \phi^{d+1}\left(\sum_i w_{ij}^{d+1} y_i^d + b_j^{d+1}\right) \quad (4)$$

In this equation, y_j^{d+1} is the output of neuron *j* in layer *d+1*, The activation function for layer *d+1*, denoted as ϕ^{d+1}, is applied to the total input received by the neuron. The term w_{ij}^{d+1} represents the weight connecting neuron *i* in layer *d* to neuron *j* in layer *d+1*, and y_i^d is the output of neuron *i* in layer *d*. The bias for neuron *j* in layer *d+1* is denoted as b_j^{d+1}.

For the hidden layer, the ReLU activation function is used, which is defined as:

$$\mathrm{ReLU}(x) = \max(x, 0) \quad (5)$$

For the output layer, a linear activation function is used, allowing the model to produce continuous output values appro-

-priate for regression tasks.

NARX networks are specifically designed to handle time series prediction problems. They account for temporal dependencies by considering both current and past input values as well as past output values. This is crucial for simulating control systems where future states depend on historical data. NARX models use their own previous outputs as part of the input for future predictions, making them highly effective for dynamic systems where the state evolves over time. The ability of NARX networks to incorporate exogenous inputs (external factors) along with autoregressive components (past values) allows them to capture complex system dynamics more effectively than simpler models.

The NARX network extends its utility to modeling nonlinear dynamic systems, incorporating dynamics at both the input layer and output feedback. n_y and n_x represent the number of output and input delays. A parallel architecture of the NARX model, as illustrated in Fig. 7, is utilized and is defined by:

$$\hat{y}(t) = F(y(t-1), y(t-2), \dots, y(t-n_y), x(t), x(t-1), \dots, x(t-n_x)) \quad (6)$$

The hyperparameters tuned for the NARX model are similar to those for the ANN, with the addition of input and output delay parameters. The most effective NARX model configuration consists of a three-layer fully connected network with twelve neurons in the hidden layer. Notably, it involves no delays in the input and features 2-time delays in the output:

$$\hat{y}(t) = F(y(t-1), y(t-2), x(t)) \quad (7)$$

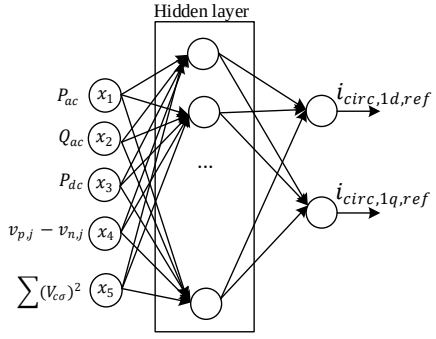

Fig. 6. The architecture of the ANN model.

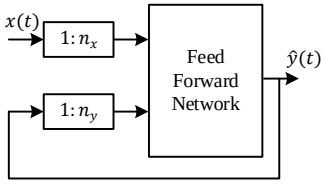

Fig. 7. The architecture of the NARX model.

E. Comparison of the Existing EBC Methods

In this evaluation, four distinct EBC methods, i.e., the conventional PI-based EBC, RF-based EBC, ANN-based EBC, and NARX-based EBC are rigorously examined and compared. This comparative analysis spans several key criteria, namely resource utilization of CPU in controller, testing MSE, memory footprint and control algorithm efficiency. Resource utilization is defined as the CPU usage percentage of the Intel Xeon processor (4 cores, 3.5 GHz) employed in the control platform during the experiments. The MSE serves as the loss function for the proposed NN-based EBC models and is a commonly used metric for evaluating neural network performance. A detailed memory footprint analysis was conducted for each control method using Linux memory profiling tools within the control platform. Note that all ML-based EBCs are trained offline, and their computational time during the inference stage is negligible. Consequently, a direct comparison of their computational speed holds limited relevance. Instead, the primary focus is on how efficiently each method leverages the computational resources provided by the CPU of the control system. Observations from TABLE 1 suggest that all four EBC methods demonstrate comparable resource utilization. However, the NARX-based EBC exhibits a slightly higher demand on computational resources. When evaluating the testing MSE of the ML-based EBC methods, the ANN model clearly outperforms the others.

Since the RF-based EBC exhibits the highest MSE on the testing dataset among the ML-based methods, the number of operating conditions in which the circulating current magnitude is smaller than the base case for the RF-based EBC was not evaluated. Consequently, its memory footprint is also not presented. All three remaining processes have similar memory footprints, with only slight variations in physical and shared memory usage. The minimal private memory usage in each case indicates that replacing the PI-based control with an ANN does not significantly increase memory consumption. In industrial applications, controllers must handle numerous functions, including protection schemes, voltage and frequency ride-through capabilities, and future upgrades. Given that the additional memory and processing power required for the ANN-based method are minimal, it is feasible to implement this method on the control platform without significant hardware modifications. Furthermore, the cost associated with upgrading controller hardware to accommodate the ANN-based method is negligible compared to the overall project costs (that include hardware and labor costs) of large-scale systems like MARS. Therefore, the ANN-based control method is practical and applicable in industrial settings.

TABLE 1 clearly highlights the advantages of the data-driven methods in terms of reducing injected fundamental circulating current. For the NARX-based EBC, 1,602 out of 2,500 operating conditions exhibit lower circulating currents compared to the PI-based EBC. Similarly, the ANN-based EBC outperforms the PI-based EBC in 1,589 operating conditions. The conduction power loss of IGBT and diode is calculated based on [37]:

$$E_{Tcond} = i_{arm}(V_{T0} + R_{CE} i_{arm})\Delta t \quad (8)$$

$$E_{Dcond} = i_{arm}(V_{D0} + R_D i_{arm})\,\Delta t \quad (9)$$

where V_{T0} and V_{D0} represent the voltage offset of the IGBT and diode, respectively, while R_{CE} and R_D denote their on-state resistances, respectively. Thus, the conduction loss of the system is directly proportional to the arm current. Since the second and fourth circulating current are suppressed to 0, smaller injected fundamental circulating current can lead to smaller conduction loss E_{cond}. This is further demonstrated by the efficiency test in Section V.A. Consequently, with reduced

circulating current under most of the operating conditions, both of these NN-based EBC methods demonstrate superior efficiency compared to the PI-based EBC.

TABLE 1
COMPARISON OF DIFFERENT EBC ALGORITHMS

	PI-based EBC	ANN-based EBC	NARX-based EBC	RF-based EBC
Testing dataset MSE	None	0.63	42.82	65.64
Resource utilization	12.7%	13.2%	13.5%	13.3%
Memory footprint (Private memory)	152 KiB	152 KiB	156 KiB	
Number of operating conditions that have a smaller circulating current magnitude than the base case	base case	1,589(out of 2,500)	1,602(out of 2,500)	

Note: The RF-based EBC's number of operating conditions and memory footprint are not presented due to their high MSE.

Beyond efficiency, another point of comparison is the number of simulations required for controller design. The PI-based EBC demands exhaustive testing. To ensure that the set of gains for the PI-based EBC can effectively balance all 2,500 operating conditions, each set of gains must undergo testing across the entire spectrum of operating conditions until stability is achieved under each one. In summary, while all three EBC methods have their merits, the NN-based EBC demonstrate superior performance. The performance of the proposed NN algorithms is showcased using the learning curve in Fig. 8 and Fig. 9, respectively.

V. INTER-PHASE AND INTER-ARM POWER MISMATCH ELIMINATION

Variations in power output of the PV arrays connected to each MARS SM could arise from factors like partial shading within the facility or malfunctioning arrays. When partial shading occurs, the affected PV SM could lead to power disparities among PV SMs within a single arm, between multiple arms, or even across different phase-legs. A novel NNPME strategy is proposed, featuring an optimization model designed to minimize PV curtailment and maximize ESS utilization. In this model, the phase power mismatch is prioritized over the arm power mismatch in the objective function, aiming to reduce the injected dc circulating current. Since the MARS system connects to both ac grids and HVdc links, three operational modes for NNPME are adapted to diverse grid requirements: fixed active power (*Pac*) mode, fixed direct current power (*Pdc*) mode, and a synergized proportional adjustment of Pac and *Pdc* mode (SPA mode), adding another layer of innovation to the proposed method.

Assume that at time $t = k$, intermittent changes in solar irradiation occur due to partial cloud coverage over specific sections of the PV plant. When this happens, a phase power mismatch emerges, characterized by the difference between the aggregated PV MPPT power of the PV SMs in any given phase, denoted as $P_{pv,MPPT,i}(k)$ where *i*=*a*,*b*,*c*, and that of the other phases. Similarly, an inter-arm power mismatch arises when the aggregated MPPT power of PV SMs in the upper arm of phase *i* differs from that of the lower arm of the same phase *i*.

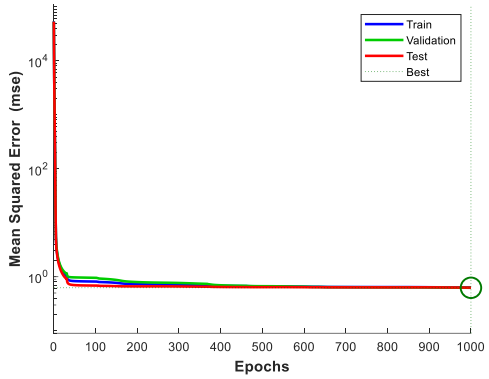

Fig. 8. Learning curve of the ANN model with the best testing performance of 0.63.

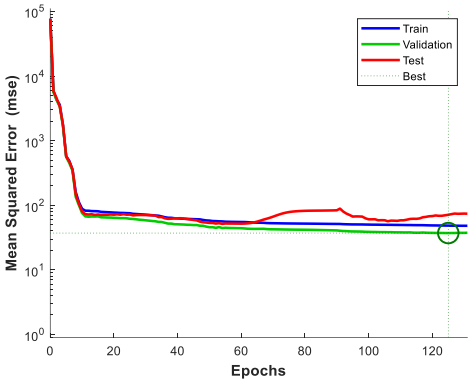

Fig. 9. Learning curve of the NARX model with the best testing performance of 42.82.

These power disparities between phases and arms impact the operation of the MARS system, leading to unbalanced SM capacitor voltages and distorted grid currents. To address this issue, the power management module in the L1 controller rearranges the dc reference power for each phase, generating a dc circulating current. This dc reference power is then fed into the dc current controller, which effectively counteracts the effects of power mismatch, ensuring balanced ac-side grid currents that meet grid code requirements. Concurrently, the ESS aids in minimizing the required dc circulating currents, thereby enhancing system efficiency and eliminating power mismatch. It is worth noting that the power references for the ESS system are constrained by $P_{ess,rating}$, which sets an upper limit on ESS power contribution.

The control algorithm for the power management module is illustrated in Fig. 10. This proposed algorithm is not only applicable to the MARS system but also to other systems featuring both PV and ESS components. Defining $d(k)$ as the change of the MARS aggregated arm PV MPPT power:

$$d(k) = Avg(P_{pv,MPPT,i})(k) - \mathrm{Avg}\left(P_{\mathrm{pv,MPPT},i}\right)(k-1) \quad (10)$$

The average PV phase power $Avg(P_{pv,MPPT,i})(k)$ is defined as:

$$Avg(P_{pv,MPPT,i})(k) = \frac{1}{3}\sum_{i=a,b,c} P_{pv,MPPT,i}\,(k)$$

$$dP_{ess,u}(k) = abs(P_{ess,rating}) + AVG\left(P_{ess,ref}(k-1)\right)$$

$$dP_{ess,l}(k) = -abs(P_{ess,rating}) + AVG\left(P_{ess,ref}(k-1)\right)$$

Upon the occurrence of a power mismatch, three distinct scenario groups will arise depending on the magnitude of changes in the average PV phase MPPT power: i) If the PV phase MPPT power change ($d(k)$) is small, then the active power and DC power can be effectively maintained using the ESS. ii) If $d(k)$ exceeds the upper limit, then curtailment is needed. iii) If $d(k)$ falls below the lower limit, then the current operating condition cannot be sustained.

i. Small changes in average PV phase MPPT power ($dP_{ess,l}(k) \le d(k) \le dP_{ess,u}(k)$).

When the change of the MARS aggregated phase PV MPPT power $d(k)$ lies between $dP_{ess,u}(k)$ and $dP_{ess,l}(k)$, the ac and average dc power commands can be maintained as:

$$P_{ac,ref}(k) = P_{ac,ref}(k-1) \quad (11)$$

$$Avg(P_{dc,ref,i,j})(k) = Avg(P_{dc,ref,i,j})(k-1) \quad (12)$$

The reference ac, dc, and ESS power will be generated according to the blue block in Fig. 10. The updated ESS power references, along with the dc circulating current references for the three phases, will be derived through an optimization algorithm. As expressed in (13), the proposed objective function consists of two terms: the first term, denoted as J_1 in (14), serves to penalize discrepancies between the dc power in each phase and the average dc power, while the second term, designated as J_2 in (15), penalizes the deviation of the dc power in each arm from the average dc power. The inclusion of both J_1 and J_2 in the objective function enables the optimization to be adaptable/applicable for a wide range of scenarios, encompassing inter-phase mismatches, inter-arm mismatches, and any possible combination thereof. The decision variable under consideration here is $P_{ess,ref,i,j}(k)$. The optimization process gives priority to minimizing the deviation of phase dc reference power, and this prioritization is reflected through a substantial weight parameter denoted as λ. This prioritization is essential as the primary objective is to minimize the required dc circulating current necessary to rectify inter-phase mismatches in the first place. If the inter-arm mismatch cannot be fully compensated by the ESS, it will be then balanced by the fundamental circulating current.

$$J_{opt} = \min_{\substack{P_{ess,ref,i,j}(k) \\ (i=a,b,c\ j=p,n)}} J_1 + J_2 \quad (13)$$

$$J_1 = \lambda \sum_{i=a,b,c}(P_{dc,ref,i}(k-1) - P_{dc,ref}(k)/3))^2 \quad (14)$$

$$J_2 = \sum_{j=p,n}^{i=a,b,c}(P_{dc,ref,i,j}(k-1) - P_{dc,ref}(k)/6))^2 \quad (15)$$

For a given $Avg(P_{dc,ref,i,j})(k)$, $P_{ess,ref,i,j}(k)$ is constrained by

$$Avg(P_{dc,ref,i,j})(k) = \sum_{j=p,n}^{i=a,b,c}\{P_{ac,ref}(k-1)/6 - P_{ess,ref,i,j}(k-1) - P_{pv,MPPT,i,j}(k-1)\} \quad (16)$$

In addition, hard constraints are imposed on the output to adhere to the operational principle of the MARS system:

$$-P_{ess,rating} \le P_{ess,ref,i,j} \le -P_{ess,rating} \quad (17)$$

Moreover, the dc reference power at each phase and the dc reference power at each arm should satisfy (15) and (16).

$$P_{dc,ref,i}(k-1) = P_{ac,ref}(k-1)/3 - P_{ess,ref,i}(k-1) - P_{pv,MPPT,i}(k-1) \quad (18)$$

$$P_{dc,ref,i,j}(k-1) = P_{ac,ref}(k-1)/6 - P_{ess,ref,i,j}(k-1) - P_{pv,MPPT,i,j}(k-1) \quad (19)$$

To sum up, the optimization model for the proposed power mismatch elimination strategy encompasses (13)-(19), which is also referred to as "optimization 1" in Fig. 10. It is solved using sequential quadratic programming (SQP).

The computational performance of the power mismatch optimization routine was assessed through offline simulations on a system with an Intel Core i7-8665U CPU operating at 1.90 GHz, with 4 cores and 8 logical processors. A 4-second offline simulation of the high-fidelity MARS model took approximately 4 hours to complete. Each simulation time step of 60 μs consumed about 0.216 seconds of real computational time in the offline simulation. Assuming an equal computational load between hardware and software computations, around 0.108 seconds per time step was allocated for software calculations in the offline simulations. The optimization computation time of 0.01 seconds represents roughly a 10% increase in the time taken to perform software computations. To meet the control platform's timestep constraints, the overall computational cost is expected to rise by approximately 10%. Implementing the optimization algorithm will thus require around 10% more computational resources compared to the controller without optimization. This slight increase in computational demand is considered acceptable, given the anticipated improvements in system performance. Additionally, as MARS is a large-scale power electronic system with significant hardware and labor costs, the expense of additional computational resources is negligible.

ii. Changes in average PV phase MPPT power exceeds the upper limit $dP_{ess,u}(k)$ ($d(k) \ge dP_{ess,u}(k)$).

In cases where the ESS charging power falls short of compensating for the increased PV power, it becomes necessary to curtail the PV power to ensure compliance with the ac and dc power commands received from the grid operator.

The PV power reference for phase *m* and arm *n*, denoted as $P_{pv,MPPT,m,n}(k)$, which has an aggregated MPPT power, exceeding the capacity of the ESS for compensation, will be adjusted. This adjustment is depicted in the green section of Fig. 10 and is then incorporated into the same optimization process described earlier.

iii. Changes in average PV phase MPPT power falls below the lower limit $dP_{ess,l}(k)$ ($d(k) \le dP_{ess,l}(k)$).

When the average arm PV MPPT power at time *k* is lower than it at previous time *k-1*, the MARS system operates in one of three modes: fixed *Pac* mode, fixed *Pdc* mode, or SPA mode. These three algorithms are depicted in the yellow blocks of Fig. 10. The symbol Δ, as defined in (20), represents the power deficit, which can result in either a reduction in ac power, an increment in dc power, or a combination of both, depending on

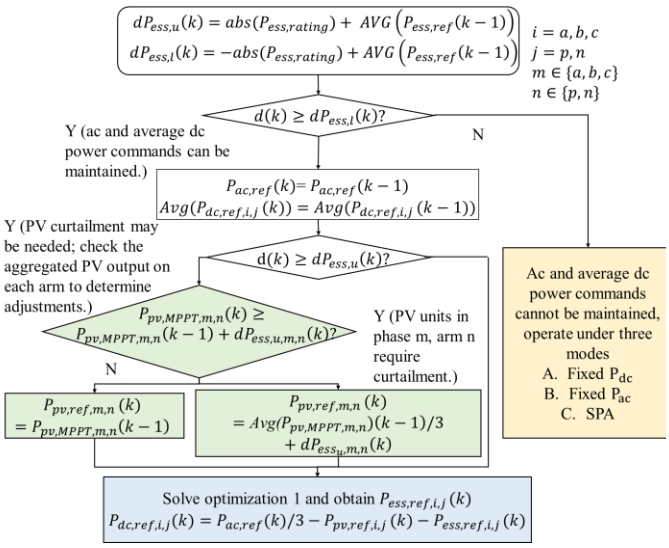

Fig. 10. Flowchart to evaluate the power reference of the PV and ESS in presence of power mismatch.

the mode of operation.

$$\Delta = -d(k) + dP_{ess,l}(k) \tag{20}$$

A. Fixed *Pac* mode

Pac needs to be maintained constant. Thus,

$$P_{ac,ref}(k) = P_{ac,ref}(k-1) \tag{21}$$

The arm average dc reference power $Avg(P_{dc,ref,i,j}(k))$ can be calcultated as

$$Avg(P_{dc,ref,i,j}(k)) = Avg(P_{dc,ref,i,j}(k-1)) - \Delta \tag{22}$$

B. Fixed *Pdc* mode

Similarly, the arm average dc reference power needs to be maintained. Thus,

$$Avg(P_{dc,ref,i,j}(k)) = Avg(P_{dc,ref,i,j}(k-1)) \tag{23}$$

Pac will be updated based on:

$$P_{ac,ref}(k) = P_{ac,ref}(k-1) - \Delta \tag{24}$$

C. SPA mode

Under SPA mode, the ratio of the ac and average dc power commands needs to be maintained. The ratio is defined as r and the $P_{ac,ref}(k)$ and $Avg(P_{dc,ref,i,j}(k))$ are updated accordingly based on:

$$P_{ac,ref}(k) = P_{ac,ref}(k-1) - r\Delta \tag{25}$$

$$Avg(P_{dc,ref,i,j}(k)) = Avg(P_{dc,ref,i,j}(k-1)) + (1-r)\Delta \tag{26}$$

The updated values of $P_{ac,ref}(k)$ and $Avg(P_{dc,ref,i,j}(k))$ are transmitted to the same optimization algorithm discussed earlier to determine the aggregated reference ESS power for each arm $P_{ess,ref,i,j}(k)$. The dc power reference for each arm that will be sent to the dc current controller is calculated as

$$P_{dc,ref,i,j}(k) = P_{ac,ref}(k)/3 - P_{pv,ref,i,j}(k) - P_{ess,ref,i,j}(k) \tag{27}$$

The proposed power management module ensures the ESSs operate at their maximum capacity while minimizing the dc circulating current injection to balance the power mismatch. Further discussion on dc-current control can be found in [5].

VI. Simulation Results

The effectiveness of the proposed NNPME strategy in addressing phase and arm power mismatches is validated through PSCAD/EMTDC simulations. The simulations utilize a test MARS system [5], featuring PV and ESS with power ratings of 100 MW and 32.8 MW, respectively, as detailed in TABLE 2. The predefined operational range of the SM capacitor voltage is between 1,280 V and 1,920 V. Deviations beyond this range are considered unacceptable.

TABLE 2

MARS System Parameters

System Parameters	Value
Simulation time-step	4 µs
System rating	400 MW
System frequency	60 Hz
Dc voltage rating	±200 kV
Ac terminal voltage	220 kV
Arm inductor	30 mH
Front-end half-bridge capacitor	7.7 mF
Nominal front-end half-bridge capacitor voltage	1.6 kV
Number of PV-SMs/arm	111
Number of ESS-SMs/arm	37
Number of normal-SMs/arm	102

A. *Efficiency test*

The ANN model is used for the efficiency test due to its superior performance in minimizing the required circulating currents and ensuring stability. An online power loss calculation is implemented in which the total power loss (Ploss_total) includes the conduction loss (Ploss_cond), switching loss (Ploss_switch), recovery loss of Diode [37], core loss [38], and inductor winding loss [39]. The PI-based EBC and NN-based EBC are tested under the operating condition of P_{ac} = 100 MW, Q_{ac} = 0, and P_{dc} = 60 MW.

It can be observed from Fig. 11 that the NN-based EBC control leads to lower power loss and higher system efficiency, achieved by injecting smaller currents and slightly sacrificing the SM capacitor voltages. Despite the higher deviation in the SM capacitor voltages, they remain within the predefined limit.

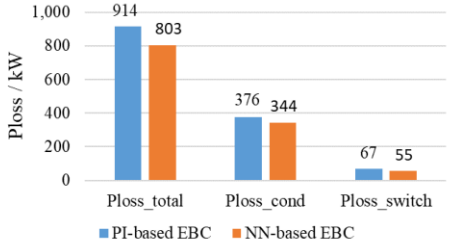

Fig. 11. Power loss comparison of PI-based EBC and NN-based EBC under one operating condition.

B. *Power Mismatch Elimination Test*

Three operation modes are considered in this paper—fixed Pac mode, fixed Pdc mode, and the SPA mode proposed in Section V. These modes are tested under both arm and phase power mismatch events. To ensure the robustness of the control system, extreme cases are examined. In this section, the fixed Pac operation mode is presented.

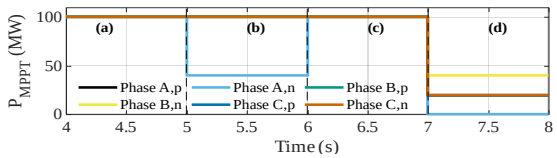

Fig. 12. Variation of P_{MPPT} per arm in response to sun irradiance change.

Fig. 12 illustrates the change in P_{MPPT} for each arm in response to changes in solar irradiance. The simulation is divided into four distinct stages.

In stage (a) (4 s~5 s), the MARS system operates at $P_{ac} = 100$ MW, $Q_{ac} = 0$, and $P_{dc} = -180$ MW, with the PV system operating at $P_{PV,MPPT} = 100$ MW and ESS is charging at 20 MW. The PV system is operating without curtailment and remains at $P_{PV,MPPT}$. During this stage, the unstable capacitor voltages shown in Fig. 13 stabilize with the assistance of the NN-based EBC, as illustrated in Fig. 14. This demonstrates the capability of the NN-based EBC in resolving inter-SM power mismatch issues.

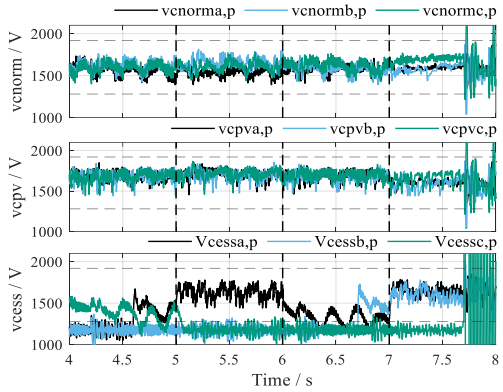

Fig. 13. The three-phase capacitor voltages of normal, PV, and ESS SMs in the upper arms, without NN-based EBC.

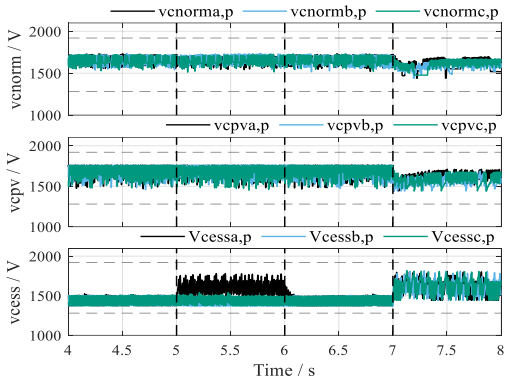

Fig. 14. The three-phase capacitor voltages of normal, PV, and ESS SMs in the upper arms, with NN-based EBC.

Stage (b) (5 s~6 s) aims to showcase the continuous and stable operation of the MARS system when an arm power mismatch occurs. At t = 5 s, the solar irradiance available to the PV arrays in phase a lower arm decreases, causing the MPPT power of phase a lower arm to change from 100/6 MW to 40/6 MW. In this case, both phase and arm power mismatches inherently exist. Since the average MPPT power of phase a satisfies $L(k) \leq Avg(P_{pv,MPPT,a})(k) \leq U(k)$, the reference power for P_{ac} and P_{dc} remains unchanged, as shown in Fig. 15 (b). Based on the dispatch command for the PV SMs and the P-V characteristics of the PV arrays, the PV-side capacitor voltages (v_{cpv}) of phase a lower arm increase to 964.7 V, while those of phase b upper and lower arms increase to 839.4 V. $P_{ess,ref}$ of phases b and c remains unchanged as the objective function prioritizes the phase mismatch, which is weighted with a large value. The ESS reference values of phase a upper and lower arms are optimized to be -12.8/6 MW and 32.8/6 MW, respectively. The changes in i_{Less} for all six arms can be observed in Fig. 15, which represent the variations in $P_{ess,ref}$.

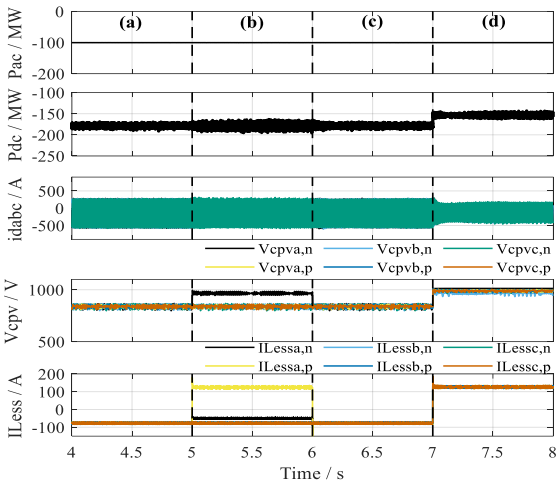

Fig. 15. Active power measured at the grid side, dc power, circulating current, capacitor voltages, and inductor current at the PV side of random PV SMs in the upper arm of the three phases.

Stage (c) represents a transitional state where the MARS system returns to the initial operating condition.

In stage (d), a scenario in which the entire area of where the PV plant is located, is assumed to be cloudy. For most of the arms, the MPPT power remains at $P_{PV,MPPT} = 20/6$ MW. Only the MPPT power of phase a lower arm and phase b lower arm are different, with $P_{PV,MPPT,a,n} = 0/6$ MW and $P_{PV,MPPT,b,n} = 40/6$ MW, respectively. In this case, $Avg(P_{pv,MPPT,i})(k) < L(\mathrm{k})$, which necessitates a change in dispatch commands according to the operation mode. The fixed Pac mode is demonstrated in Fig. 15 (d), where Pac remains constant while P_{dc} increases to compensate for Pac. The increase in i_{dabc} during mismatch events can be attributed to the fact that the fundamental circulating current required for the initial operating condition to balance the inter-SM mismatch is significantly higher than the circulating current needed to compensate for the inter-arm mismatch. Furthermore, the operating condition in stage (d) necessitates a lower circulating current to balance the inter-SM mismatch than in stage (a). As $P_{PV,MPPT}$ decreases, V_{cpv} increases. All ESS units charge at their $P_{ess,rating}$ to compensate for the loss of solar irradiation, as shown in the i_{Less} of Fig. 15 (d). Fig. 13 (d) illustrates that capacitor voltages begin to diverge without the presence of the NN-based EBC, highlighting the crucial role of the NN-based EBC in resolving the inter-arm power mismatches.

VII. cHIL Results

The presented results are per unitized, with the base power rating of the system at 400 MW, the base L-L voltage at 220 kV, the base dc current at 1 kA and the base SM capacitor voltage at 1.6 kV. The cHIL tests are used to evaluate the robustness of the NN-EBC under stable operating conditions, and grid events. The cHIL platform consists of the control system of the MARS that connects to the real-time simulator hardware through actual communication interfaces [40]. This

cHIL platform incorporates communication delays and the essential data processing inherent in a realistic control system, aspects that are challenging to replicate in offline simulations.

The general specification of the control platform and real time simulator used in the cHIL is shown in TABLE 3.

TABLE 3

SPECIFICATIONS OF THE CONTROL PLATFORM AND REAL-TIME SIMULATOR

	control platform	real time simulator
CPU	Intel Xeon CPU E3-1275 v5, 4 cores, 3.5 GHz	Intel® Xeon® E5 series, 2x8 Cores, 3.2 GHz
FPGA	Xilinx Kintex™-7 325T	Xilinx® Virtex®-7 FPGA, 485T

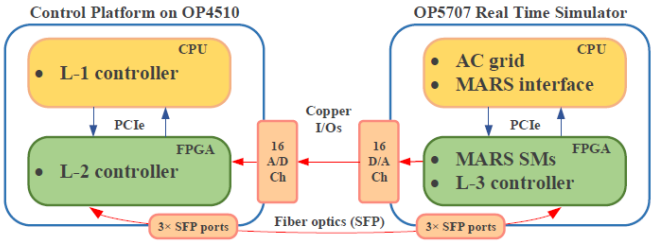

Fig. 16. Diagram of the cHIL system setup.

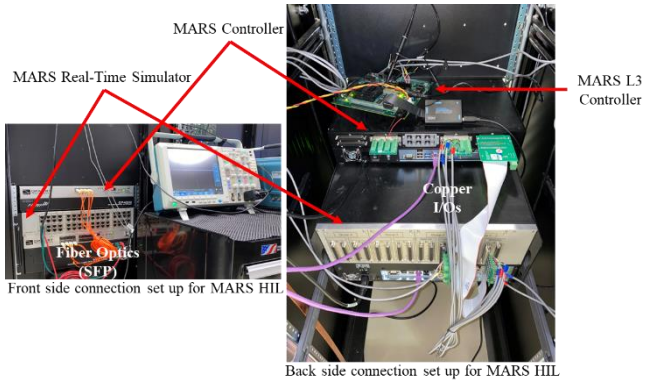

Fig. 17. The MARS cHIL test layout.

The cHIL setup, depicted in Fig. 16, incorporates the slower components such as ac grid model and the MARS ac interface model, which are implemented in the central processing unit (CPU) of real-time simulator and simulated at a time step of 60 μs. The MARS converter, including the front-end half-bridge circuits, and normal, PV, and ESS SMs, along with their L3 controllers, are implemented in the Xilinx Virtex-7 Field Programmable Gate Arrays (FPGA) of real-time simulator. The control system has the L2 controller implemented in its FPGA and the L1 controller in a CPU. The control system of the MARS and the real-time simulation hardware of the MARS are interconnected to each other with both fiber optics (for SFP) as well as copper conductors (for analog I/Os) to exchange various signals. The actual cHIL setup is displayed in Fig. 17.

A. Transition from Conventional Sorting Algorithm to NN-based EBC under Unstable Operating Conditions

In this case study, the cHIL tests initially run with the EBC disabled, using only the conventional sorting algorithm to balance the SM capacitor voltages. Subsequently, the tests are conducted with the NN-based EBC enabled. The test results are shown in Fig. 18, where the dispatched ac-side power command

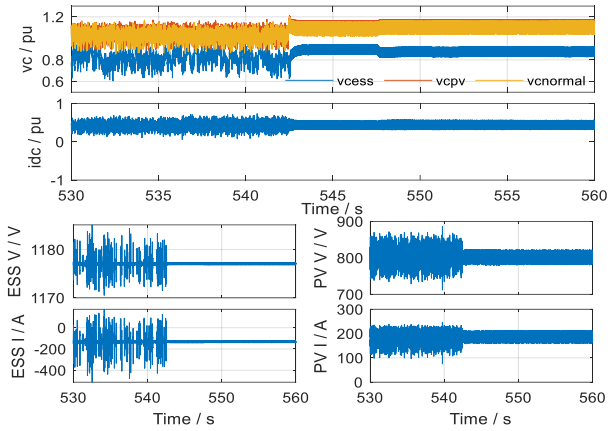

Fig. 18. SM capacitor voltages of three types of SMs as well as capacitor voltages of the ESS and PV dc-dc converters and their inductor currents under the operating condition of P_{ac} = 0.25 pu, Q_{ac} = 0.125 pu, and P_{dc} = 0.15 pu.

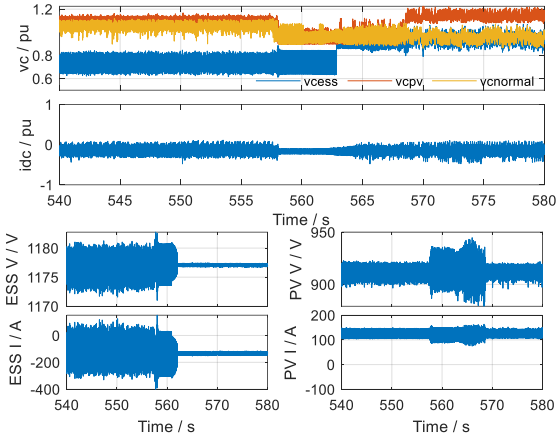

Fig. 19. SM capacitor voltages of three types of SMs as well as capacitor voltages of the ESS and PV dc-dc converters and their inductor currents under the operating condition of P_{ac}= -0.25 MW, P_{dc}= -0.425 MW, and Q_{ac}= 0.

is set at P_{ac} = 0.25 pu, Q_{ac} = 0.125 pu, and P_{dc} = 0.15 pu. The PV and ESS dc-dc converters are activated and connected to the MARS system, with the PV reference voltage of 810 V and ESS reference discharging power of -150 kW. As shown in Fig. 18, the SM capacitor voltages of the front-end half-bridge circuits are initially unbalanced when the EBC is disabled, and the ESS SM capacitor voltages fall outside the specified range of 0.8~1.2 pu. This condition leads to instability in the L3 ESS controller. Subsequently, upon enabling the NN-based EBC, the SM capacitor voltages become balanced. A negative power dispatch is sent to the MARS under operating conditions P_{ac}= -0.25 MW, P_{dc}= -0.425 MW, and Q_{ac}= 0. The SM capacitor voltages initially fall outside the specified range when the EBC is disabled. However, with EBC enabled, the ESS SM capacitor voltages are effectively brought back within the pre-defined range, as shown in Fig. 19. This demonstrates that the EBC is functioning well under these operating conditions and helps maintain SM capacitor voltages across different types of SMs.

B. Operating Condition Changes

The performance of the proposed NN-based EBC under various operating conditions is presented in Fig. 20. A cyclic test is performed, involving dispatch command steps

transitioning form P_{ac} = 0.75 pu, Q_{ac} = 0, and P_{dc} = 0.75 pu (stable without the EBC) to P_{ac} = 0.375 pu, Q_{ac} = 0.5 pu, and P_{dc} = 0.375 pu (unstable without the EBC), P_{ac} = 0.25 pu, Q_{ac} = -0.125 pu, and P_{dc} = 0.15 pu (unstable without the EBC), P_{ac} = -0.125 pu, and Q_{ac} = 0, P_{dc}= -0.185 pu (unstable without the EBC) (unstable without the EBC) and back to the first operating condition. The results of the cyclic test, performed under different operating conditions with the NN-based EBC included in the control are presented in Fig. 20. The measured grid-side active and reactive powers are effectively controlled to match the references. Throughout these changes in operating conditions, the grid-side currents remain stable. Furthermore, all three types of SM capacitor voltages are balanced and remain within the pre-defined range, demonstrating successful operation of the NN-based EBC.

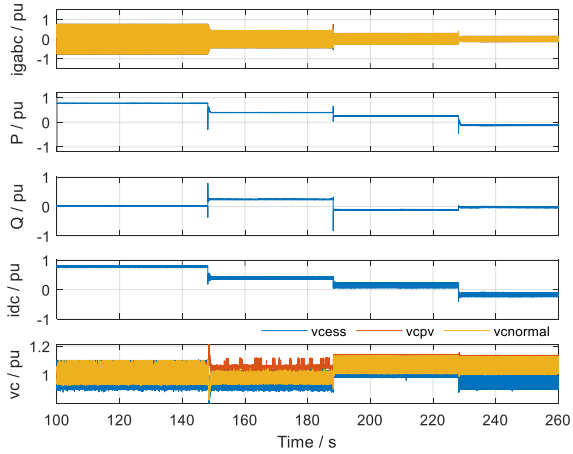

Fig. 20. Measured MARS grid-side currents, active and reactive powers, dc current, and capacitor voltages in the representative SMs subsequent to changes in the operating condition.

C. Robustness of the NN-based EBC Evaluated under Different Grid Events

The proposed NN-based EBC is evaluated under two common grid events under multiple operating conditions. The two events include: (a) A 804.44 MW loss of generation based on Haynes3 generator in the WECC grid, and (b) a balanced three-phase fault with a duration of 0.2 s, and (c) a line-to-line fault with a duration of 0.2 s. The VSG in the L1 controller provides both frequency and voltage support, ensuring continuity of operation of the MARS during grid events. In this section, only the cHIL test results corresponding to the operating condition $P_{ac} = 0.25$ pu, $Q_{ac} = 0$, and $P_{dc} = 0.25$ pu are presented. As evidenced by Fig. 21, Fig. 22, and Fig. 23, the SM capacitor voltages of different types of SMs consistently remain within the predefined upper and lower limits throughout these grid events. The ac-side currents remain sinusoidal and balanced without encountering any instability issue. Similar tests were conducted under other stressed operating conditions to further examine the stability of the controller. This also serves as validation of the real-time calculation capabilities of the NN-based EBC, showcasing its reliability and effectiveness in handling grid disturbances.

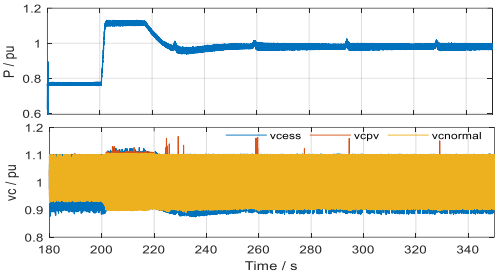

Fig. 21. Active power measured at the MARS terminal, and the capacitor voltages of different types of SMs during a loss of generation event.

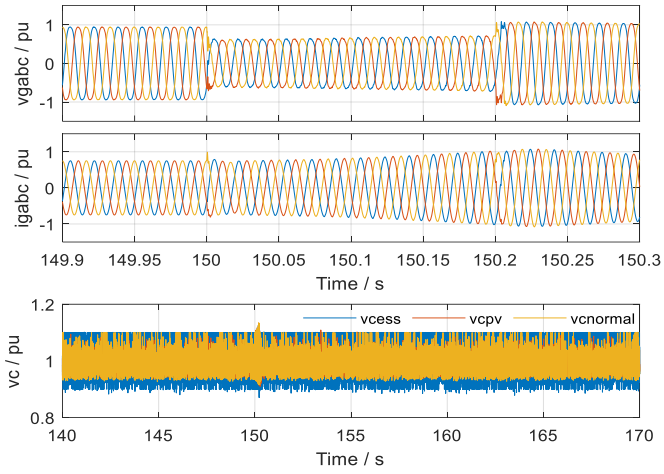

Fig. 22. Ac-side currents and voltages, and capacitor voltages of different types of SMs during a three-phase fault event.

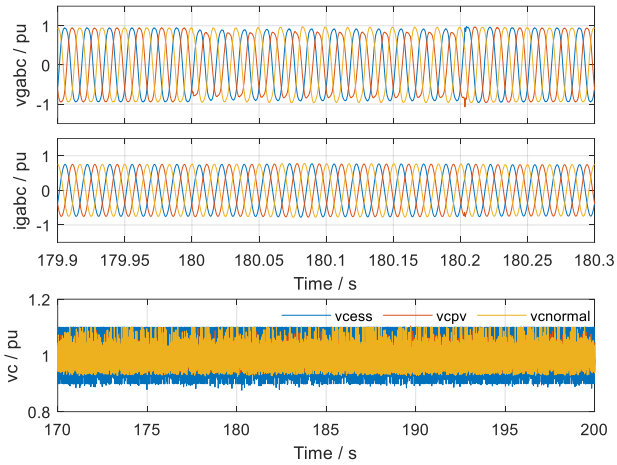

Fig. 23. Ac-side currents and voltages, capacitor voltages of different types of SMs during a line-to-line fault event.

VIII. Conclusion

In this paper, a NNPME comprising of a power management module and an NN-based EBC, is developed to ensure stable operation of the MARS system under various operating conditions. The proposed NN-based EBC outperforms the benchmark PI-based EBC, as it adeptly handles circulating current references, efficiently addresses power mismatches and preserves capacitor voltage balance without the need for any complex tuning process. This paper also presents an analytical analysis for inter-SM, inter-phase, and inter-arm power mismatch elimination. Inter-arm and inter-phase power mismatches are tested based on the PSCAD/EMTDC

simulations. Simulation results demonstrate successful operation of the proposed NNPME strategy under partial shading conditions. Additionally, the cHIL experimental results indicate that the proposed method can achieve SM capacitor voltage balancing under various grid events and operating conditions, showcasing its stability and feasibility as an advanced control solution for MARS-type systems. In summary, the proposed NNPME is particularly useful when a power mismatch exists within the converter and can be applied to other three-phase converter topologies where energy sources, such as PV, batteries, and wind, are connected to submodules. Additionally, it enables the connection of differently rated renewable systems, like PV, within a single MMC arm, offering flexibility for future expansions and the integration of renewable energy sources.

REFERENCES

[1] G. Wang *et al*., "Power smoothing of large solar PV plant using hybrid energy storage," in *IEEE Transactions on Sustainable Energy*, vol. 5, no. 3, pp. 834–842, Jul. 2014

[2] Y. Yang *et al*., "Integrated Size and Energy Management Design of Battery Storage to Enhance Grid Integration of Large-Scale PV Power Plants," in *IEEE Transactions on Industrial Electronics*, vol. 65, no. 1, pp. 394-402, Jan. 2018.

[3] G. Konstantinou *et al*., "A hybrid modular multilevel converter with partial embedded energy storage," in *Energies*, vol. 9, no. 12, pp. 1012–1029, Sep. 2016.

[4] J. I. Leon *et al*., "Multilevel converters: Control and modulation techniques for their operation and industrial applications," in *Proc. IEEE*, vol. 105, no. 11, pp. 2066–2081, Nov. 2017.

[5] S. Debnath *et al*., "Renewable Integration in Hybrid AC/DC Systems Using a Multi-Port Autonomous Reconfigurable Solar Power Plant (MARS)," in *IEEE Transactions on Power Systems*, vol. 36, no. 1 2021.

[6] G. Liang *et al., "*Analytical Derivation of Inter-submodule Active Power Disparity Limits in Modular Multilevel Converter-Based Battery Energy Storage Systems," in *IEEE Transactions on Power Electronics*, vol. 36, no. 3, pp. 2864-2874, March 2021.

[7] T. Soong *et al*., "Internal Power Flow of a Modular Multilevel Converter with Distributed Energy Resources," in *IEEE Journal of Emerging and Selected Topics in Power Electronics*, vol. 2, no. 4, Dec. 2014.

[8] H. Kim *et al*., "Operating Region of Modular Multilevel Converter for HVDC With Controlled Second-Order Harmonic Circulating Current: Elaborating P-Q Capability," in *IEEE Transactions on Power Delivery*, vol. 31, no. 2, pp. 493-502, April 2016.

[9] Z. Yang *et al*., "A Control Strategy for Suppressing Submodule Capacitor Voltage Fluctuation of MMC Based on Circulating Current Voltage Drop Balance," in *IEEE Access*, vol. 9, pp. 9130-9141, 2021.

[10] Y. Yi *et al*., "Branch Voltage Balancing Control Strategy Based on the Transfer Power Model by Zero-Sequence Circulating Current for the Hexverter," in *IEEE Access*, vol. 10, pp. 44326-44336, 2022.

[11] F. Briz *et al*., "Operation and control of MMCs using cells with power transfer capability," *IEEE Applied Power Electronics Conference and Exposition (APEC)*, Charlotte, NC, USA, 2015, pp. 980-987.

[12] X. Pan *et al*., "Decoupling Capacitor Minimization of an MMC-Based Photovoltaic System with Three-Winding Power Channel," in *IEEE Transactions on Power Electronics*, vol. 37, no. 1, Jan. 2022.

[13] J. Liu, T. Wei, N. Chen, W. Liu, J. Wu, and P. Xiao, "A neural network PID controller with dynamic structure adjustment for DC-DC switching converters," in Proc. IEEE 7th Int. Conf. Integr. Circuits Microsystems, 2022, pp. 356–360.

[14] S. Sahoo, H. Wang and F. Blaabjerg, "On the Explainability of Black Box Data-Driven Controllers for Power Electronic Converters," *2021 IEEE Energy Conversion Congress and Exposition (ECCE)*, Vancouver, BC, Canada, 2021, pp. 1366-1372.

[15] X. Liu, L. Qiu, Y. Fang and J. Rodríguez, "Predictor-Based Data-Driven Model-Free Adaptive Predictive Control of Power Converters Using Machine Learning," in *IEEE Transactions on Industrial Electronics*, vol. 70, no. 8, pp. 7591-7603, Aug. 2023.

[16] S. Wang, T. Dragicevic, Y. Gao and R. Teodorescu, "Neural Network Based Model Predictive Controllers for Modular Multilevel Converters," in *IEEE Transactions on Energy Conversion*, vol. 36, no. 2, pp. 1562-1571, June 2021.

[17] S. Wang, T. Dragicevic, G. F. Gontijo, S. K. Chaudhary and R. Teodorescu, "Machine Learning Emulation of Model Predictive Control for Modular Multilevel Converters," in *IEEE Transactions on Industrial Electronics*, vol. 68, no. 11, pp. 11628-11634, Nov. 2021.

[18] D. Wang *et al*., "Model Predictive Control Using Artificial Neural Network for Power Converters," in *IEEE Transactions on Industrial Electronics*, vol. 69, no. 4, pp. 3689-3699, April 2022.

[19] X. Liu et al., "Neural Predictor-Based Low Switching Frequency FCS-MPC for MMC With Online Weighting Factors Tuning," in *IEEE Transactions on Power Electronics*, vol. 37, no. 4, pp. 4065-4079, April 2022.

[20] P. Poblete, G. Pizarro, G. Droguett, F. Núñez, P. D. Judge and J. Pereda, "Distributed Neural Network Observer for Submodule Capacitor Voltage Estimation in Modular Multilevel Converters," in *IEEE Transactions on Power Electronics*, vol. 37, no. 9, pp. 10306-10318, Sept. 2022.

[21] L. Tong, Y. Chen, T. Xu and Y. Kang, "Fault Diagnosis for Modular Multilevel Converter (MMC) Based on Deep Learning: An Edge Implementation Using Binary Neural Network," in *IEEE Journal of Emerging and Selected Topics in Power Electronics*, vol. 11, no. 6, pp. 5553-5568, Dec. 2023.

[22] C. Fan, K. Xiahou, L. Wang and Q. H. Wu, "Hybrid Fault Diagnosis of Multiple Open-Circuit Faults for Cascaded H-Bridge Multilevel Converter Based on Perturbation Estimation Convolution Network," in *IEEE Transactions on Instrumentation and Measurement*, vol. 73, pp. 1-12, 2024.

[23] S. Wang *et al*., "Neural Network Based Model Predictive Controllers for Modular Multilevel Converters," in *IEEE Transactions on Energy Conversion*, vol. 36, no. 2, pp. 1562-1571, June 2021.

[24] E. Gümrükcü *et al*., "Optimal Management for Megawatt Level Electric Vehicle Charging Stations with a Grid Interface Based on Modular Multilevel Converter," in *IEEE Access*, vol. 10, pp. 258-270, 2022.

[25] H. Bayat and A. Yazdani, "A Power Mismatch Elimination Strategy for an MMC-Based Photovoltaic System," in *IEEE Transactions on Energy Conversion*, vol. 33, no. 3, pp. 1519-1528, Sept. 2018.

[26] J. Yu, Z. Liu, J. Kong, J. Gong, L. Ding and S. Lu, "A Novel Integrating Configuration and A Power Distribution Method for MMC-Based Grid-Connected PV System with Integrated Batteries," *46th Annual Conference of the IEEE Industrial Electronics Society (IECON)*, Singapore, 2020, pp. 3164-3169.

[27] H. Bayat and A. Yazdani, "A Hybrid MMC-Based Photovoltaic and Battery Energy Storage System," in *IEEE Power and Energy Technology Systems Journal*, vol. 6, no. 1, pp. 32-40, March 2019.

[28] S. Rivera *et al*., "Modular multilevel converter for large-scale multistring photovoltaic energy conversion system," in *IEEE Energy Conversion Congress and Exposition*, 2013, pp. 1941-1946.

[29] A. Elsanabary, S. Mekhilef, M. Seyedmahmoudian and A. Stojcevski, "A Novel Circuit Configuration for the Integration of Modular Multilevel Converter with Large-Scale Grid-Connected PV Systems," in *IEEE Transactions on Energy Conversion*, vol. 39, no. 1, pp. 3-16, March 2024.

[30] A. Elsanabary, S. Mekhilef and N. F. A. Aziz, "Internal Power Balancing of an MMC-Based Large-Scale PV System under Unbalanced Voltage Sags," in *IEEE Journal of Emerging and Selected Topics in Power Electronics.* PP. 1-1. 10.1109/JESTPE.2024.3399395.

[31] Y. Pan, X. Sun, Y. Cai, X. Li and W. Zhao, "An Improved Coordination Control for Enhancing Photovoltaic Power Imbalance Tolerant Capability of MMC-Based Photovoltaic System," in *IEEE Transactions on Power Electronics*, vol. 39, no. 9, pp. 11732-11745, Sept. 2024.

[32] S. Nayak and A. Das, "A Power Balancing Strategy in a PV-Based Modular Multilevel Converter During Mismatched Power Generation," in *IEEE Transactions on Industrial Electronics*, vol. 71, no. 7, pp. 7117-7125, July 2024.

[33] F. Rong *et al*., "A Novel PV System Based on MMC to Get the Maximum Power Under Partial Shading Conditions," in *IEEE Transactions on Power Electronics*, vol. 32, no. 6, pp. 4320-4333, June 2017.

[34] W. Li *et al*., "A Modular Multilevel Converter Pulse Generation and Capacitor Voltage Balance Method Optimized for FPGA Implementation," in *IEEE Transactions on Industrial Electronics*, vol. 62, no. 5 May 2015.

[35] IEEE Standard for Harmonic Control in Electric Power Systems," in *IEEE Std 519-2022 (Revision of IEEE Std 519-2014)*, pp.1-31, Aug. 2022.
[36] Cigre Working Group B4.68. DC Side Harmonics and Filtering in HVDC Transmission Systems; Cigre Working Group B4.68: Paris, France, 2020.
[37] Y. Shiyuan *et al*., "Instantaneous Power Loss Calculation for MMC Based on Virtual Arm Mathematical Model," *International Power Electronics Conference (IPEC ECCE Asia)*, Niigata, Japan, 2018.
[38] W. Shen, F. Wang, D. Boroyevich and C. W. Tipton, "Loss Characterization and Calculation of Nanocrystalline Cores for High-frequency Magnetics Applications," *IEEE Applied Power Electronics Conference and Exposition*, Anaheim, CA, USA, 2007, pp. 90-96.
[39] R. P. Wojda and M. K. Kazimierczuk, "Magnetic Field Distribution and Analytical Optimization of Foil Windings Conducting Sinusoidal Current," in *IEEE Magnetics Letters*, vol. 4, pp. 0500204-0500204, 2013.
[40] Z. Dong *et al*., "Real-time Simulation Framework for Hardware-in-the-Loop Testing of Multi-port Autonomous Reconfigurable Solar Power Plant (MARS)," *IEEE Energy Conversion Congress and Exposition (ECCE)*, Vancouver, BC, Canada, 2021, pp. 3160-3167.

Qianxue Xia (Member, IEEE) She received the Ph.D. degree in electrical engineering from in electrical engineering at Georgia Institute of Technology in 2022. Currently, she is a postdoctoral researcher at Oak Ridge National Laboratory, Knoxville, TN, USA. Her main research interests are in artificial intelligence application in control and modeling of power electronics.

Suman Debnath (Senior member, IEEE) received the Ph.D. degree in electrical engineering from Purdue University, West Lafayette, IN, USA, in 2015. Currently, he is a Senior R&D staff at Oak Ridge National Laboratory, Knoxville, TN, USA. His main research interests are in applied mathematics for high-fidelity modeling and advanced simulation algorithms for electromagnetic transient [EMT] simulation.

Maryam Saeedifard (Fellow, IEEE) received the Ph.D. degree in electrical engineering from the University of Toronto, Toronto, ON, Canada, in 2008. She is currently a Ken Byers Professor with the School of Electrical and Computer Engineering, Georgia Institute of Technology, Atlanta, GA, USA. Her research interests include power electronics and applications of power electronics in power systems.